Supplemental Material for "Signatures of ultrafast reversal of excitonic order in Ta_2NiSe_5"

H. Ning,[1,2] O. Mehio,[1,2] M. Buchhold,[1,2] T.Kurumaji,[3] G. Refael,[1,2] J. G. Checkelsky,[3] and D. Hsieh[1,2]

[1]*Institute for Quantum Information and Matter, California Institute of Technology, Pasadena, CA 91125*
[2]*Department of Physics, California Institute of Technology, Pasadena, CA 91125*
[3]*Department of Physics, Massachusetts Institute of Technology, 77 Massachusetts Ave., Cambridge, MA 02139*

Contents

I. Derivation of the microscopic dynamical equations 1

II. Determination of the microscopic parameters 3

III. Difference between the calculated and experimental critical fluence 4

IV. Ultrafast heating and subsequent cooling 4

V. Non-monotonic behavior of the OPCP amplitude versus fluence above the critical fluence 5

VI. ISRS/DECP phonon simulation 6

VII. Experiment and fitting details 6

VIII. Detailed comparison of double-pump experiment and simulation 8

References 8

I. DERIVATION OF THE MICROSCOPIC DYNAMICAL EQUATIONS

In order to connect the dynamics of the OPCP and the exciton condensate with the microscopic description of Ta_2NiSe_5, we start from a commonly used two-band semiconductor Hamiltonian with spinless fermions [1–4] and inter-band interactions,

$$H = \sum_k (\epsilon_k {c_k}^\dagger c_k + \mu_k {v_k}^\dagger v_k) + \sum_i (V {c_i}^\dagger c_i {v_i}^\dagger v_i + \omega_0 {b_i}^\dagger b_i + g({b_i}^\dagger + b_i)({c_i}^\dagger v_i + {v_i}^\dagger c_i)) \quad (1)$$

The bands are formed by the quasi-one-dimensional lattice and i, k are the corresponding lattice sites and momentum. Each operator and parameter is defined in the main text. We also set $\hbar = 1$ for simplicity.

The equations of motion for the complex exciton order parameter $\Phi_i = \langle c_i^\dagger v_i \rangle$ and the real lattice displacement $X_i = \langle b_i^\dagger + b_i \rangle$ can be obtain by expressing Eq. (1) in terms of a nonequilibrium path integral (i.e. in the Keldysh framework) and introducing Φ as a dynamic, bosonic Hubbard-Stratonovich field. This allows one to integrate out the fermionic modes and derive the equations of motion for Φ, X via saddle point equations.

In a path integral approach, the partition function Z corresponding to the Hamiltonian in Eq. (1) is formally obtained from a field integral of the form

$$Z = \int \mathcal{D}[\{\bar{c}_i, c_i, \bar{v}_i, v_i, b_i^*, b_i, \Phi_i^*, \Phi_i\}] e^{iS}, \quad (2)$$

where $\mathcal{D}$ represents the common field integral measure and $\bar{c}_i, c_i, \bar{v}_i, v_i$ are independent Grassmann fields, representing the fermion modes in conduction and valence bands, and $b_i^*, b_i, \Phi_i^*, \Phi_i$ are complex fields, corresponding to the phonon and exciton condensate modes. The Keldysh action S is obtained in the canonical way [5] and reads as $S = S_\mathrm{f} + S_\mathrm{b}$ with the fermion part

$$S_\mathrm{f} = \sum_{l,m} \int_t \bar{\Psi}_{l,t} \begin{pmatrix} C^{-1}_{l,m,t} & M_{l,t}\delta_{l,m} \\ M^*_{l,t}\delta_{l,m} & W^{-1}_{l,m,t} \end{pmatrix} \Psi^T_{m,t} \quad (3)$$

and the boson part

$$S_\mathrm{b} = \sum_l \int_t \Big[(b^*_{c,l,t}, b^*_{q,l,t}) B^{-1}_{l,t} \begin{pmatrix} b_{c,l,t} \\ b_{q,l,t} \end{pmatrix} - V \left(\Phi^*_{c,l,t}\Phi_{q,l,t} + \Phi^*_{q,l,t}\Phi_{c,l,t} \right) \Big]. \quad (4)$$

Here, $\Psi_{l,t} = (c_{1,l,t}, c_{2,l,t}, v_{1,l,t}, v_{2,l,t})$ is the fermion spinor in Keldysh space and each field carries an index triplet (i, l, t), which labels Keldysh component i ($i = 1, 2$ for Grassmann fields and $i = c, q$ for complex fields), lattice site l and time t. The matrices B, C, W are the Keldysh space Green's function for phonons, conduction band, and valence band. They are diagonal in frequency and momentum space

$$C^{-1}_{k,\omega} = \begin{pmatrix} 0 & \omega - \epsilon_k - i\eta \\ \omega - \epsilon_k + i\eta & 2i\eta \tanh(\omega/2T) \end{pmatrix} \quad (5)$$

and $W^{-1}_{k,\omega}$ is identical with $\epsilon_k \to \mu_k$. Also,

$$B^{-1}_{k,\omega} = \begin{pmatrix} 0 & \omega - \omega_0 - i\eta \\ \omega - \omega_0 + i\eta & 2i\eta \tanh(\omega/2T) \end{pmatrix} \quad (6)$$

with $\eta \to 0^+$. The matrix $M_{l,t}$ describes the local coupling of the fermions to the exciton and phonon fields

$$M_{l,t} = \left[\mathbf{1}\left(V\Phi_{c,l,t} + gX_{c,l,t}\right) + \sigma_x\left(V\Phi_{q,l,t} + gX_{q,l,t}\right)\right]. \tag{7}$$

The fermion part S_f is quadratic in Grassmann fields and integration according to Grassmann calculus yields the formal expression

$$S_\mathrm{f} = -i\mathrm{Tr}\left(\log\left[\mathbf{1} - CMWM^*\right]\right) = i\sum_{n=1}^{\infty}\frac{1}{n}\mathrm{Tr}\left(CMWM^*\right)^n, \tag{8}$$

where the trace includes the sum over Keldysh indices and lattice sites and an integral over time. In order to eliminate the phonon field from the nonlinear action S_f, one performs a polaron-type shift $\Phi_{c/q,l,t} \to \Phi_{c/q,l,t} - \frac{g}{V}X_{c/q,l,t}$. For small exciton field amplitudes Φ, Eq. (8) can be expanded up to fourth order in the fields ($n \leq 2$) and in powers of derivatives. The equations of motion for the exciton condensate and the displacement, which are represented by the classical fields $\Phi_{c,l,t}, X_{c,l,t}$ are obtained via the saddle-point equations (and their complex conjugates)

$$\frac{\delta S}{\delta b_{q,l,t}} = \frac{\delta S}{\delta \Phi_{q,l,t}} = 0. \tag{9}$$

This yields the equations of motion by further introducing the perturbation of light via Peierls substitution, which is argued to work better for an electronically localized system [4], and assuming the lattice constant $d = 1$:

$$iZ\partial_t\Phi = (-\tilde{D}(\nabla - iqA)^2 + \tilde{m} + \tilde{U}|\Phi|^2)\Phi + \frac{2g}{V}X, \tag{10}$$

$$\partial_t{}^2X = -({\omega_0}^2 + \frac{2g^2\omega_0}{V})X - 2g\omega_0\,\mathrm{Re}(\Phi), \tag{11}$$

with the parameters $\tilde{D}, \tilde{m}, \tilde{U}, Z$ depending on integrals over Green's functions and therefore on the band structure of the material and the temperature T of the system. Assuming a band gap Δ and $k_BT < \Delta$, i.e. negligible population in the conduction bands, we can write out these parameters

$$\tilde{m} = 1 - \frac{2V}{\sqrt{\Delta(2J_c + 2J_v + \Delta)}}, \tag{12}$$

$$\tilde{D} = \frac{2J_cJ_vV}{\sqrt{\Delta(2J_c + 2J_v + \Delta)}^3}, \tag{13}$$

$$Z = V\left(\frac{2J_c + 2J_v + 2\Delta}{\sqrt{\Delta(2J_c + 2J_v + \Delta)}^3}\right), \tag{14}$$

$$\tilde{U} = \left(\frac{2(3(J_c + J_v)^2 + 4\Delta(J_c + J_v) + 2\Delta^2)}{\sqrt{\Delta(2J_c + 2J_v + \Delta)}^5}\right)V^3. \tag{15}$$

The equations in the main text are obtained via $m = \tilde{m}/Z$, $U = \tilde{U}/Z$, $D = \tilde{D}/Z$, $g' = g/(ZV)$, and $f = \tilde{D}q^2A^2/Z \triangleq \alpha F\exp\left(-\frac{4\ln 2t^2}{\sigma^2}\right)$.

Also, we can obtain real valued equations of motion by defining $\Phi = \phi + i\eta$. To characterize the dephasing of the phononic and electronic channels, we also add phenomenological decaying terms to both branches. It is straightforward to add a $-2\gamma_{ph}\partial_tX$ term to the structural dynamical equation and γ_{ph} can be determined experimentally. For the complex electronic order parameter, on the other hand, we rewrite the order parameter dynamical equation as followed:

$$i\partial_t\Phi = ((-D(\nabla - iqA)^2 + m + U|\Phi|^2)\Phi + 2g'X)(1 - i\gamma_e), \tag{16}$$

Here γ_e is dimensionless. It expresses the ratio of dephasing dynamics due to a non-zero temperature to the coherent dynamics of the order parameter. Both dynamics are generated by the same effective free energy functional. It determines the dephasing time of the electronic Higgs/Goldstone oscillations as validated in Section II.

Also, we ignore the spatial diffusion and the phonon frequency shift due to an order of magnitude estimate $g \approx \omega_0 \ll V$. With all of the above rectifications we have:

$$\partial_t\phi = (f + m + U(\phi^2 + \eta^2))\eta - \gamma_e((f + m + U(\phi^2 + \eta^2))\phi + 2g'X), \tag{17}$$

$$\partial_t\eta = -(f + m + U(\phi^2 + \eta^2))\phi - 2g'X - \gamma_e(f + m + U(\phi^2 + \eta^2))\eta, \tag{18}$$

$$\partial_t{}^2X = -{\omega_0}^2X - 2g\omega_0\phi - 2\gamma_{ph}\partial_tX. \tag{19}$$

We then construct the initial conditions for the above equations, which guarantee that X is static and Φ remains real and static before the light excitation:

$$\phi|_{t=0} = \sqrt{\frac{4gg'/\omega_0 - m}{U}}. \tag{20}$$

$$\eta|_{t=0} = 0. \tag{21}$$

$$\partial_tX|_{t=0} = 0, \tag{22}$$

$$X|_{t=0} = -\frac{2g}{\omega_0}\sqrt{\frac{4gg'/\omega_0 - m}{U}}, \tag{23}$$

After establishing the equations and the initial conditions, we can numerically solve the differential equations and trace the dynamics of the complex electronic order parameter Φ and the real structural order parameter X [Fig. S1], as well as the dynamical free energy landscapes. By taking the fast Fourier transform (FFT) of X in the time interval from 0 ps to 20 ps with different pumping fluence values, we obtain the order-parameter-coupled phonon (OPCP) amplitude versus fluence curves [Fig. S2].

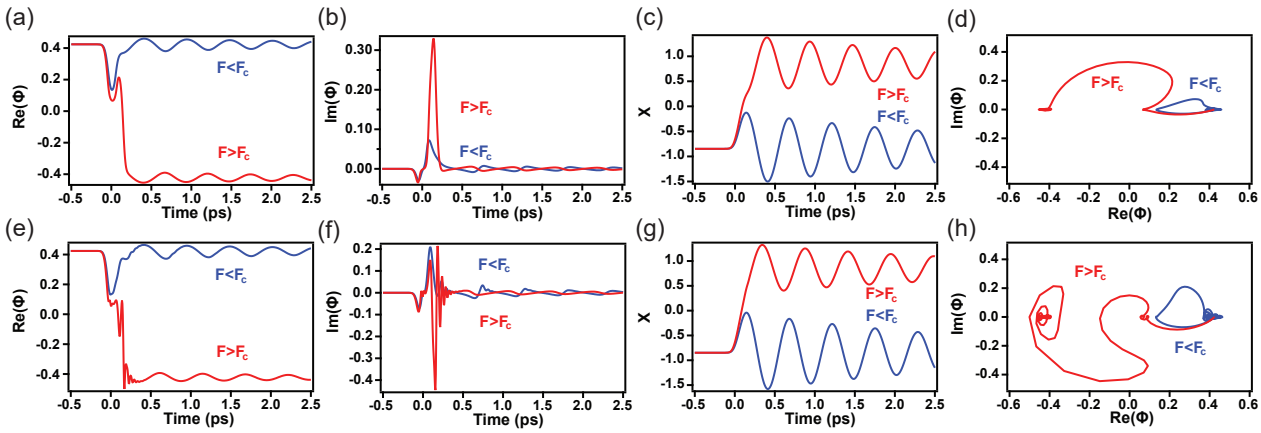

FIG. S1: Simulated time evolution of the electronic and lattice order parameters in the (a)-(d) overdamped (γ_e=1) and (e)-(h) underdamped (γ_e=0.1) cases. In each case, data are shown with fluences below and above the critical fluence, and the model parameters are set to $\omega_0/(2\pi) = 2$ THz, $g = 2$ THz, $V = 60$ THz, $\Delta = J_c = J_v = 40$ THz, and $\gamma_{ph} = 0.3$ THz. (a),(e) Time evolution of the real part of the electronic order parameter. (b),(f) Time evolution of the imaginary part of the electronic order parameter. (c),(g) Time evolution of the lattice order parameter. (d),(h) Trajectory of the electronic order parameter.

To simulate the two-pulse pumping situation, one simply adds another f term to Eq. (17) and (18) that is identical to the first, except that this f term is centered at the time when the second pulse arrives at the sample. The initial conditions are the same. Here we apply a FFT to X in the time interval between the arrival of the second pulse and 20 ps thereafter. We thus obtain the OPCP amplitude versus fluence at different time delays [Fig. S5].

II. DETERMINATION OF THE MICROSCOPIC PARAMETERS

From our experiment we get $\omega_0/(2\pi) = 2$ THz. The chosen microscopic parameter values in Ref.[3, 4] reproduce the equilibrium band structure qualitatively well, therefore we adopt these and set $g = 2$ THz, $V = 60$ THz, $\Delta = 40$ THz, $J_c = J_v = 40$ THz, $m = -17$ THz, $U = 132$ THz, $D = 13.3$ THz, and $g' = 0.83g$. The Higgs mode frequency $-2m = 34$ THz qualitatively matches the gap size Δ [6]. The corresponding fast oscillation is beyond the time resolution of our experimental setup, and hence cannot be resolved. The phonon dephasing time we measured is approximately 3 ps, thus $\gamma_{ph} \approx 0.3$ THz. This set of parameter choices is self-consistent but may not be unique. We also demonstrate that the specific choice of the above microscopic parameters does not change the main conclusion of this paper, i.e. the reversal of the EI order [Fig. S2(b)]. We simulate our incident light as a $\sigma = 100$ fs Gaussian irradiating the sample at $t = 0$. The pump fluence F is thus the only tunable parameter.

There is uncertainty in the determination of the electron decay rate γ_e. Recent theories have demonstrated that the electronic system can oscillate in an amplitude (Higgs) and phase (Goldstone) mode around the transient free energy minimum [3], but there is no experimental evidence of such modes so far. A large γ_e describes the overdamped case where the electronic subsystem adiabatically evolves into the transient free energy minimum, while a small γ_e captures the underdamped case where Φ explores a larger region of the Mexican-hat potential via rapid oscillations of the Higgs and the Goldstone modes upon light excitation [Fig. S1(h)]. We demonstrate that the nature of the electronic decay, whether overdamped or underdamped, does not change our main finding, i.e. the reversal of the EI order and the concurrent anomalous phonon amplitude dependence. We simulated the aforementioned two cases using either $\gamma_e = 1$, which typically characterizes an overdamped scenario with no oscillation [Fig. S1(a)-(d)], or $\gamma_e = 0.1$, which describes the underdamped case [Fig. S1(3)-(h)]. With $\gamma_e = 0.1$, the rapid Higgs/Goldstone oscillation clearly damps out in 0.25 ps. Despite the distinction in γ_e, the dynamics of Φ and X are comparable qualitatively at times longer than 0.25 ps after the light excitation. The clear reversal when the pump fluence is higher than the critical fluence is realized independent of the value of γ_e. Further, alteration of the electron dephasing rate has a minimal affect on the reversal critical fluence [Fig. S2(a)]. Since an investigation of the behavior of the Higgs/Goldstone mode is beyond the scope of this work, we only simulate with the overdamped case hereafter.

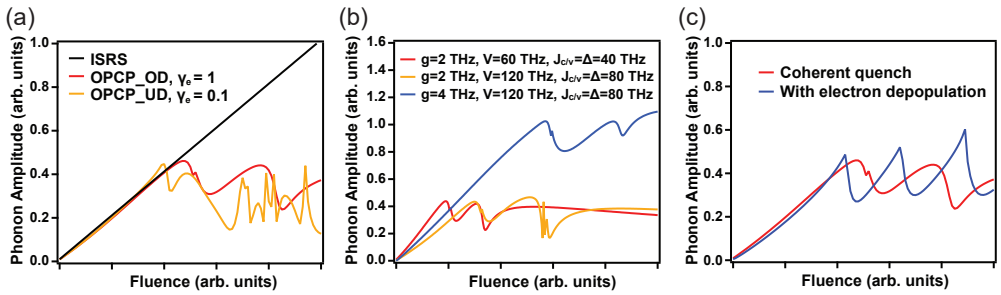

FIG. S2: Fluence dependence of the OPCP with various choices of the microscopic model parameters. (a) OPCP amplitude versus fluence with different electronic decay times. The red curve corresponds to the overdamped case ($\gamma_e = 1$) and the yellow curve corresponds to the underdamped case ($\gamma_e = 0.1$) with $g = 2$ THz, $V = 60$ THz, $\Delta = J_c = J_v = 40$ THz. The black curve characterizes the ISRS/DECP amplitude versus fluence. (b) OPCP amplitude versus fluence in the overdamped case ($\gamma_e = 1$) with different choices of g, V, Δ, J_c, J_v. (c) OPCP amplitude versus fluence in the overdamped case with or without considering the depopulation time of the electrons, with the same model parameters as in (a).

III. DIFFERENCE BETWEEN THE CALCULATED AND EXPERIMENTAL CRITICAL FLUENCE

In Section I, we defined $f \triangleq \alpha F \exp\left(-\frac{4 \ln 2 t^2}{\sigma^2}\right)$. To get the value of the simulated critical fluence F_c in real units, we explicitly write out the scaling factor $\alpha = \frac{8Dq^2d^2(1-R)}{\hbar^2{\omega_{ph}}^2 c\epsilon_0\sigma}$, where D is the parameter defined in Section I, q is electron charge, d is the lattice constant, R is the reflectance, $\hbar$ is the reduced Planck's constant, ω_{ph} is the pump light frequency, c is the speed of light, ϵ_0 is the vacuum permittivity, σ is the pulse duration. Our model predicts that F_c should be smaller when the pump polarization is parallel to the chain direction because d is smaller and R is larger in this geometry. This is consistent with the data reported in Ref. [6].

We obtained a simulated $F_c \sim 6$ mJ/cm^2 under the same reported experimental conditions [6], which needs to be scaled down by 16 times to match the real experimental F_c. There are several possible factors that give rise to this discrepancy. First, our model is an elementary model with a simplified two-band structure. There are also uncertainties in the determination of the parameters J_c, J_v, Δ, g, and V. It is especially hard to determine g and V from experiment because they are not directly reflected in band structure measurements. Even though the chosen parameter values in Ref.[3, 4] are claimed to reproduce the experimental data well in Ref. [7], we find the band dispersions displayed in several other ARPES papers differ subtly, giving rise to an uncertainty in the determination of the parameters [8–11]. In Fig. S2(b) we show several OPCP amplitude versus pumping fluence curves obtained using different sets of parameter choices. It is clear that F_c changes with the value of the microscopic parameters, but the qualitative trend stays the same.

Second, F_c is temperature-dependent. Increasing temperature makes the bandwidth and bandgap smaller and the Mexican-hat minimum shallower, both of which promote the order-parameter switch, thereby decreasing F_c. Our simulation corresponds to $T = 0$ K case, and therefore gives an upper bound of F_c. As shown in Ref. [6], a 100 K increase in the temperature can make F_c several times smaller. As such, it is possible that F_c at finite temperature is much smaller than 0 K. To give an accurate estimate, a temperature dependent model needs to be considered.

Third, transient heating effects are not accounted for in our model. For pump photon energies above the insulating gap, which is the case in our experiment, there will be finite absorption leading to transient heating of the electronic subsystem. This will contribute towards quenching the electronic potential in a similar manner to coherent electric field driving. Therefore neglecting transient heating effects will cause F_c to be over-estimated. On the other hand, this approximation may be more realistic for the case of sub-gap pumping where absorption is suppressed.

Taken altogether, these three factors lead us to conclude that our microscopic model and the corresponding simulation qualitatively reproduce the experimental observation. We also emphasize that regardless of the choice of parameters, the anomalous behavior of an OPCP is well reproduced in all simulations, demonstrating our conclusions are robust against the specific value of the parameters.

IV. ULTRAFAST HEATING AND SUBSEQUENT COOLING

We note that ultrafast heating and subsequent cooling in both the electronic and structural channels upon pumping are not considered in our coherent-drive microscopic model. We demonstrate here that ignoring the heating and the subsequent cooling does not change the major conclusions.

We first consider the electronic channel. Upon pumping, the electrons are excited into the conduction bands and the effective electronic temperature increases dramatically. The ultrafast heating of the electrons is accompanied by the transient restoration of higher symmetry, i.e. Mexican hat becomes parabolic, producing a qualitatively similar effect to that imparted by our coherent driving model. In both cases, one can deterministically engineer the final state through pumping. In our model we introduce light perturbation via a coherent Peierls phase, implying an immediate relaxation to lower symmetry as soon as the pulse excitation is over. Although this theoretical treatment is extensively utilized, in reality hot electrons will thermalize with the lattice through EPC with a characteristic depopulation time of 1 ps in Ta_2NiSe_5 as measured by time-resolved optical and electron spectroscopy [6–10, 12]. This implies the higher symmetry exists beyond the time duration of the pulse. To take this depopulation time into account, we simulate the pulse as a 1 ps exponential decay convolved with a Gaussian. The dynamics of the order parameters are very similar to the dynamics in the coherent quench case, except for the fact that the order parameters reach their stable states after longer time (1-2 ps) due to thermalization. We show the OPCP fluence dependence with thermalization in Fig. S2(c). Compared with the coherent quench case, the switch to the counterpart state occurs at a slightly lower fluence but the trend is the same. Therefore, we conclude here that the heating and cooling of the electrons do not influence our major conclusion that the switch is achievable by increasing fluence and observable via the OPCP fluence dependence.

To estimate the lattice heating, we use the formula $\Delta T = \frac{(1-R)F}{C\rho\delta}$ to calculate the lattice effective temperature increase, where R is the reflectance, ρ is the density, C is the specific heat capacity, and δ is the optical penetration depth for the pump photon energy (1 eV) [13, 14]. Our experiments were performed at 80 K with a pump fluence of 0.5 mJ/cm^2. Using these values, we obtain a temperature increase of 15 K. Therefore, the lattice temperature is far below T_c after pumping and the lattice temperature induced change of band structure is negligible. Thus, the lattice heating can also be ignored.

V. NON-MONOTONIC BEHAVIOR OF THE OPCP AMPLITUDE VERSUS FLUENCE ABOVE THE CRITICAL FLUENCE

As depicted in Fig. S2, the OPCP amplitude as a function of pump fluence shows a non-monotonic behavior when $F > F_c$. The amplitude of the "oscillation" and the fluence where they emerge are dependent on the specific values of the microscopic parameters. This behavior arises from the strong feedback between the electronic and structural order parameter dynamics immediately after excitation. Because Φ always responds more rapidly than X, the subtle mismatch of the time when the two order parameters cross zero will influence the phonon amplitude.

We take the case with overdamped dynamics as an example. In such a case, Φ relaxes into the potential minimum instantaneously, while X takes a longer time to settle into the minimum depending on the phonon damping rate. When the pump fluence just surpasses F_c, once the pump excitation is over and X starts to approach zero from the negative side, Re(Φ) does not cross zero but exhibits a partial regression back to the initial state [Fig. S1(a) and (c)]. This incomplete return to the initial state in turn tilts the phonon potential in the opposite direction as X is evolving, thus exerting resistance to the phonon and decreasing the phonon amplitude. However, as the pump fluence further increases, X crosses zero more quickly and the aforementioned temporal mismatch between X and Φ crossing zero will be smaller, leading to a slight increase of the phonon amplitude. This explains the non-monotonic behavior that occurs just above F_c in Fig S2(a). After careful examination of the dynamics of both channels at each pump fluence, we find that this temporal mismatch occurs twice as the pump fluence is increased, yielding the two "dips" above F_c in the overdamped cases [Fig. S2(a) and (b)]. The "dips" finally disappear after the pump fluence is high enough so that Φ directly crosses zero without returning partially back to the initial state. Thereafter X and Φ will not experience any mismatch and the phonon amplitude shows a smooth monotonic dependence on fluence.

The non-monotonic behavior is stronger for the underdamped case because Φ undergoes Higgs/Goldstone oscillations [Fig. S2(a)]. The feedback between the two channels thus also lasts longer, creating more complicated dynamics. In addition to the mismatch between the time when X and Φ cross zero as discussed in the overdamped case, the order parameters can now also oscillate back-and-forth between the minima on either side of zero [Fig. S1(e)-(h)]. This makes the final state more sensitive to pump fluence compared to the overdamped case. In other words, the order parameter is more susceptible to reversal upon small changes in pump fluence, leading to sharper modulations of the phonon amplitude.

We also note that in the overdamped case where we account for electronic heating and cooling, increasing pump fluence will induce a greater number of reversals back to the initial state within one phonon period (0.5 ps), and the oscillations in Fig. S2(c) actually stem from these back-and-forth reversals. In contrast, the reversal only occurs once in the overdamped coherent pumping case. This discrepancy reveals that the long-time dynamics of the coupled system is strongly influenced by the dynamics immediately after the excitation. While these differences lead to quantitatively different long time behaviors, they do not alter the main conclusion of this

work, i.e. the observation of the first reversal and the non-monotonic behavior of the OPCP amplitude versus fluence above F_c.

VI. ISRS/DECP PHONON SIMULATION

As mentioned in the main text, conventional Raman active phonon modes are launched through the impulsive stimulated Raman scattering (ISRS) or displacive excitation of coherent phonons (DECP) mechanisms. Several references have discussed and summarized the disparities between and the unification of these two mechanisms [15–18]. We simulated conventional ISRS/DECP phonons using the simplified formula from [19]:

$$\partial_t{}^2 X = -{\omega_{ph}}^2 X - 2\gamma_{ph}\partial_t X + F(t) \tag{24}$$

where in the displacive case, $F(t) = D\theta(t)$ and in the impulsive case $F(t) = F\delta(t)$. Convolving with the Gaussian-envelope pulse we have $F(t) = D\frac{1+\mathrm{erf}\,(\sqrt{\frac{4\ln(2)}{\sigma^2}}t)}{2}$ for the DECP case and $F(t) = F\exp(-\frac{4\ln(2)t^2}{\sigma^2})$ for the ISRS case, where D and F are normalized fluences. The dynamics for both cases are generally the same except for a $\pi/2$ phase shift. As shown in Fig. S2(a), the amplitude of the ISRS/DECP-launched phonon has a linear fluence dependence.

VII. EXPERIMENT AND FITTING DETAILS

Single crystals of Ta_2NiSe_5 were grown by chemical vapor transport reaction. First, a powder of Ta_2NiSe_5 was synthesized by the solid-state reaction from a stoichiometric mixture of its elements. They were sealed in an evacuated quartz tube and heated at 900 ℃ for 5 hours. Next, the powder (around 2 g) and chunks of iodine (50 mg) were loaded in a sealed quartz tube, which was put in a two-zone furnace. The temperature for the growth sides were kept at 875 ℃ and 800 ℃ respectively for one month. The samples were cleaved along the (010) direction immediately before the experiment to obtain a fresh and smooth surface.

For double-pump experiments, the sample temperature was fixed at 80 K. In the experimental setup, a Ti:sapphire amplified laser operating at 1 kHz produces 800 nm pulses with 40 fs time duration. A small portion of the power is used as the probe. The remainder seeds an optical parametric amplifier (OPA) and generates near infrared light tuned to 1200 nm with a duration of 80 fs, which is used for the the pump pulse(s). The fluence of each pump was set to ∼0.5 mJ/cm^2, which is around F_c at 80 K, considering the temperature dependence of F_c [6]. Our simulation further substantiates that the fluence is slightly below F_c as shown later. The polarizations of both pulses were set to be perpendicular to the (100) axis

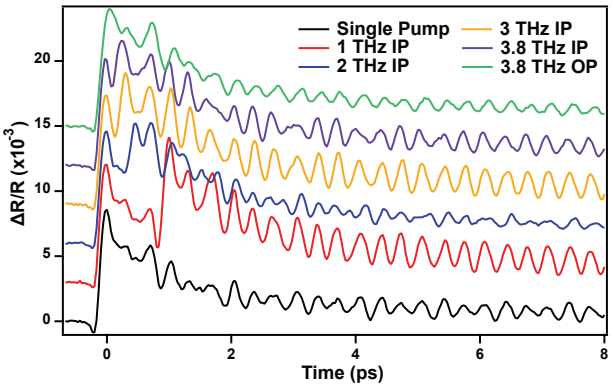

FIG. S3: Transient reflectivity in response to both a single pump (black) and two pumps (other colors). In the double-pump data, the delays between the two pumps are set to be either in-phase (IP) or out-of-phase (OP) with a certain phonon, as indicated in the legend. Each curve is vertically offset for clarity.

of the sample, since pumping with a parallel polarization was reported to generate phonons less efficiently [6].

Transient differential reflectivity curves with double- and single-pump are shown in Fig. S3. All curves exhibit a clear beat pattern. The quick rise upon the arrival of the pump and the ensuing exponential decay (∼ 1 ps) characterize photocarrier generation and recombination respectively, in agreement with previous results [6, 12]. The beat pattern indicates the coexistence of multiple coherent phonons. Three phonons centered at around 2 THz, 3 THz and 3.8 THz are identified after taking the fast Fourier transforms (FFT) of the transient reflectivity data, as depicted in Fig. S4. The reported 1 and 4 THz phonons are missing [9, 10, 12].

To test whether we are able to amplify or suppress the different observed phonons, we excite the sample with two pump pulses with the time delay between them tuned to be either in-phase (IP) and out-of-phase (OP) with each phonon respectively. As such, there are six configurations in total. Note that when the time delay is IP with the 2 THz phonon, it is nearly OP with the 3 THz phonon. Similarly, when the time delay is IP with the 3.8 THz phonon, it is nearly OP with the 2 THz phonon. Therefore, two configurations are redundant and we executed the double-pump experiment using 4 different fixed delays between the two pumps. The corresponding double-pump FFT spectra are displayed in Fig. S4, together with the single pump FFT spectrum. In Fig. S4(b), it is demonstrated that when the time delay between the two pump pulses is resonant with the 3 THz phonon, the 3 THz phonon amplitude is amplified by almost two times. Simultaneously, the 3.8 THz phonon is slightly enhanced because this time delay is also partially IP with its period, while the 2 THz phonon is suppressed due to the nearly OP time delay. Similar

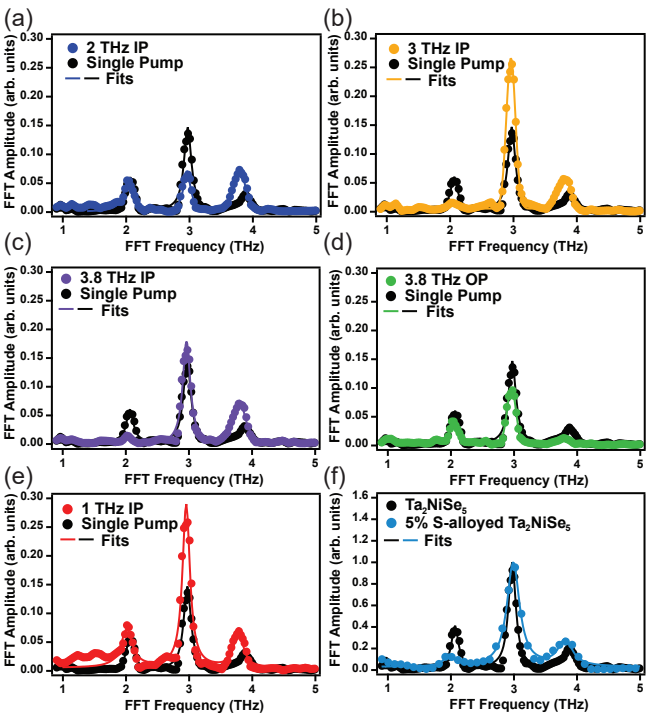

FIG. S4: FFTs of experimental double- and single-pump transient reflectivity data taken on pristine and 5% S-alloyed Ta_2NiSe_5. All FFTs are taken in the time interval between 0 ps and 8 ps. (a - e) FFT spectra of the traces shown in Fig. S3. The black dots correspond to the spectrum of the single pump excitation, shown in each panel as a reference, while the dots of other colors indicate the spectra of the double-pump data. The solid lines correspond to the Lorentzian fits. (f) Single-pump FFT spectrum for a 5% S-alloyed Ta_2NiSe_5 (cyan) with the data on the pristine sample as a reference (black).

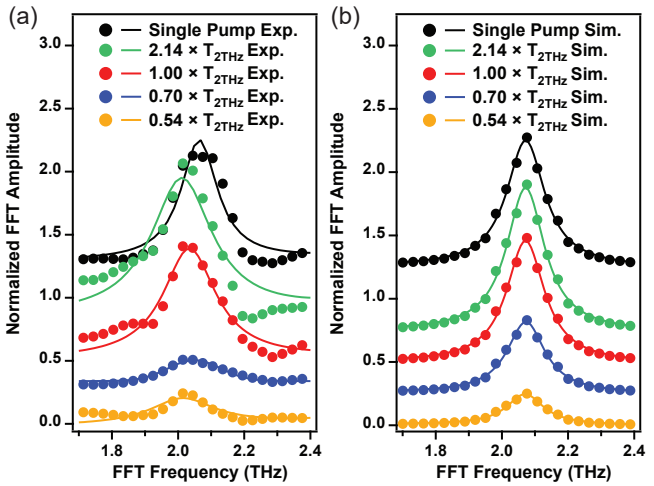

FIG. S5: FFT spectra of the 2 THz phonon obtained from (a) experiment and (b) simulation of the microscopic model at time delays equal to $2.14 \times T_{2THz}$ (green, corresponds to the 1 THz IP pumping), $1 \times T_{2THz}$ (red, corresponds to the 2 THz IP pumping), $0.7 \times T_{2THz}$ (blue, corresponds to the 3 THz IP pumping), and $0.54 \times T_{2THz}$ (yellow, corresponds to the 3.8 THz IP pumping). The single pump results are displayed as a reference. Each curve is vertically offset for clarity and normalized by the peak value of the single pump FFT.

analysis can be used to interpret the 3.8 THz IP and OP pumping cases in Fig. S4(c) and S4(d). However, an anomalous behavior is observed in the 2 THz IP pumping configuration as shown in Fig. S4(a). Although the 3 THz phonon is suppressed due to the OP time delay, and the 3.8 THz phonon is amplified due to nearly IP pumping, the 2 THz phonon is not enhanced.

The reported 1 THz OPCP [6] is missing in our single-pump spectrum. Fig. S4(e) displays the FFT spectrum of the 1 THz IP pumping. 1 THz IP pumping should be nearly IP with all the phonons, but only the 3 THz and 3.8 THz phonon are amplified. There is still no 1 THz phonon after pumping resonantly with it, and the enhancement of the 2 THz phonon is negligible, echoing the 2 THz IP double-pump results. Similar results were reproduced at different spots on two samples. This further demonstrates the 2 THz phonon is an OPCP unlike the 3 THz and 3.8 THz phonons.

We also conducted coherent phonon spectroscopy measurement on 5% S-doped Ta_2NiSe_5. The FFT spectrum shows a much weaker 2 THz phonon than the undoped case, but similarly intense 3 THz and 3.8 THz phonons, as shown in Fig. S4(f). This observation is further evidence that the 2 THz phonon is coupled to the EI order while the 3 and 3.8 THz phonons are not, since S-doped Ta_2NiSe_5 exhibits weaker EI order with a lower T_c [14].

In principle we can fit the time traces with damped oscillations superposed atop an exponentially decaying background:

$$\frac{\Delta R}{R} = A\exp\left(-\frac{t}{\tau_0}\right)+C+\sum_i B_i \exp\left(-\frac{t}{\tau_{ph,i}}\right)\cos\left(\nu_i t+\phi_i\right) \tag{25}$$

where A denotes the electronic background amplitude due to photocarrier generation with a decay time τ_0, and C characterizes the long heat escape time. B_i, $\tau_{ph,i}$, ν_i, ϕ_i are the amplitude, lifetime, frequency and phase of the ith phonon respectively. Here i runs from 1 to 3 corresponding to 2, 3 and 3.8 THz phonons.

Equivalently, we can also fit the peaks in the FFT spectrum. A damped oscillation in the time domain transforms into a Lorentzian in the frequency domain. Thus, we can fit the FFT data with three Lorentzians with the same definition of the corresponding parameters as defined above:

$$\sum_i \frac{B_i}{(\nu-\nu_i)^2+(1/2\tau_{ph,i})^2} \tag{26}$$

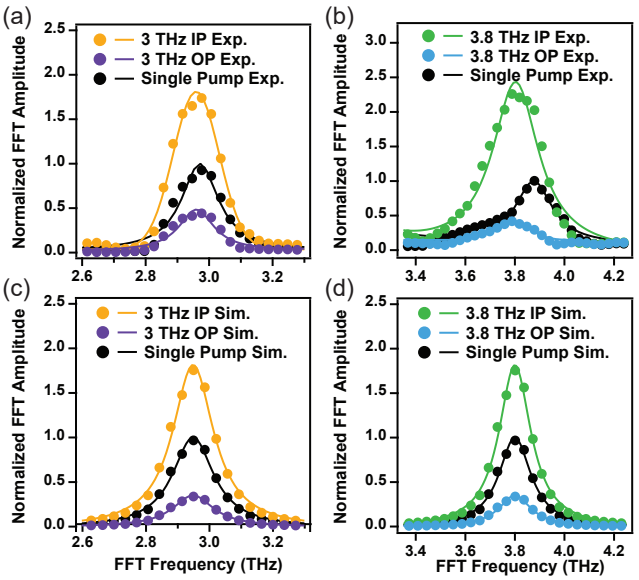

FIG. S6: FFT spectra of the (a) 3 THz and (b) 3.8 THz phonons obtained from experimental data with IP and OP pumping. FFT spectra of the (c) 3 THz and (d) 3.8 THz phonons obtained from simulation results with IP and OP pumping. The single pump result is displayed in each panel (black) as a reference. Each curve is normalized by the peak value of the single pump FFT.

VIII. DETAILED COMPARISON OF DOUBLE-PUMP EXPERIMENT AND SIMULATION

Here we present a detailed comparison between experiment and simulation of the complete pump time-delay dependence of the 2 THz phonon in the double-pump scheme. We zoom in on the 2 THz phonon FFT peak at the aforementioned five different time delays as shown in Fig. S5(a). Note that the time delays are expressed as multiples of the 2 THz phonon period (T_{2THz}). We simulated the time evolution of X upon two-pulse excitation using the same time delays as in our double-pump experiment and obtained a FFT spectrum for each delay. The simulation results using a pump fluence $F = 0.96F_c$ per pulse reproduce the experimental data well [Fig. S5(b)]. Simulation with pump fluence $F > F_c$ fails to reproduce the experimental data even qualitatively.

As a comparison, the 3 THz and 3.8 THz phonons exhibit enhancement with IP pumping and suppression with OP pumping, resembling the ISRS simulation very well [Fig. S6] and thus demonstrating their uncoupled nature. Also note that the measured frequency of all three phonons after double-pumping redshifts compared with the single-pump case due to higher net pumping fluences [Fig. S5 and Fig. S6]. This softening may come from carrier-excitation-induced lattice softening and phonon anharmonicity [20–22], which are ignored in our microscopic model and unrelated to the main results.

[1] B. Zenker, H. Fehske, and H. Beck, Phys. Rev. B **90**, 195118 (2014).
[2] Y. Tanaka, M. Daira, and K. Yonemitsu, Phys. Rev. B **97**, 115105 (2018).
[3] Y. Murakami, D. Golež, M. Eckstein, and P. Werner, Phys. Rev. Lett. **119**, 247601 (2017).
[4] T. Tanabe, K. Sugimoto, and Y. Ohta, Phys. Rev. B **98**, 235127 (2018).
[5] A. Kamenev, *Field Theory of Non-Equilibrium Systems* (Cambridge University Press, 2011).
[6] D. Werdehausen, T. Takayama, M. Höppner, G. Albrecht, A. W. Rost, Y. Lu, D. Manske, H. Takagi, and S. Kaiser, Sci. Adv. **4** (2018), eaap8652.
[7] S. Mor, M. Herzog, D. Golež, P. Werner, M. Eckstein, N. Katayama, M. Nohara, H. Takagi, T. Mizokawa, C. Monney, and J. Stähler, Phys. Rev. Lett. **119**, 086401 (2017).
[8] K. Okazaki, Y. Ogawa, T. Suzuki, T. Yamamoto, T. Someya, S. Michimae, M. Watanabe, Y. Lu, M. Nohara, H. Takagi, N. Katayama, H. Sawa, M. Fujisawa, T. Kanai, N. Ishii, J. Itatani, T. Mizokawa, and S. Shin, Nature Communications **9**, 4322 (2018).
[9] T. Tang, H. Wang, S. Duan, Y. Yang, C. Huang, Y. Guo, D. Qian, and W. Zhang, arXiv:2003.00514 .
[10] T. Suzuki, Y. Shinohara, Y. Lu, M. Watanabe, J. Xu, K. L. Ishikawa, H. Takagi, M. Nohara, N. Katayama, H. Sawa, M. Fujisawa, T. Kanai, J. Itatani, T. Mizokawa, S. Shin, and K. Okazaki, arXiv:2002.10037 .
[11] M. D. Watson, I. Marković, E. A. Morales, P. L. Fèvre, M. Merz, A. A. Haghighirad, and P. D. C. King, arXiv:1912.01591 .
[12] S. Mor, M. Herzog, J. Noack, N. Katayama, M. Nohara, H. Takagi, A. Trunschke, T. Mizokawa, C. Monney, and J. Stähler, Phys. Rev. B **97**, 115154 (2018).
[13] T. I. Larkin, A. N. Yaresko, D. Pröpper, K. A. Kikoin, Y. F. Lu, T. Takayama, Y.-L. Mathis, A. W. Rost, H. Takagi, B. Keimer, and A. V. Boris, Phys. Rev. B **95**, 195144 (2017).
[14] Y. F. Lu, H. Kono, T. I. Larkin, A. W. Rost, T. Takayama, A. V. Boris, B. Keimer, and H. Takagi, Nature Communications **8**, 14408 (2017).
[15] H. J. Zeiger, J. Vidal, T. K. Cheng, E. P. Ippen, G. Dresselhaus, and M. S. Dresselhaus, Phys. Rev. B **45**, 768 (1992).
[16] A. V. Kuznetsov and C. J. Stanton, Phys. Rev. Lett. **73**, 3243 (1994).
[17] T. E. Stevens, J. Kuhl, and R. Merlin, Phys. Rev. B **65**, 144304 (2002).
[18] A. Melnikov, O. Misochko, and S. Chekalin, Physics Letters A **375**, 2017 (2011).
[19] O. V. Misochko and M. V. Lebedev, Phys. Rev. B **94**, 184307 (2016).
[20] S. Hunsche, K. Wienecke, T. Dekorsy, and H. Kurz, Phys. Rev. Lett. **75**, 1815 (1995).
[21] P. Tangney and S. Fahy, Phys. Rev. Lett. **82**, 4340 (1999).
[22] M. Hase, M. Kitajima, S.-i. Nakashima, and K. Mizoguchi, Phys. Rev. Lett. **88**, 067401 (2002).